Efficient Pr₂NiO₄@Pr₆O₁₁ (PPNO) composite cathode synthesized via reactive magnetron sputtering (RMS) for MS-SOFC applications

Xiaolei YE ^{a,b}, Jiyun GAO^c, Shenghui GUO^{a,b,*}, Ming HOU^{a,b}, Li Yang ^{a,b}, Lei GAO^{a,b}, Kaihua CHEN ^{a,b,*}, Yunchuan LI ^{a,b}, Pascal BRIOIS^d

- ^a Faculty of Metallurgical and Energy Engineering, Kunming University of Science and Technology, Kunming 650093, China
- ^b State Key Laboratory of Complex Nonferrous Metal Resources Clean Utilization, Faculty of Metallurgical and Energy Engineering, Kunming University of Science and Technology, Kunming 650093, China
- ^c School of Chemistry and Environment, Yunnan Minzu University, Kunming 650093, China
- ^d FEMTO-ST Institute (UMR CNRS 6174), UBFC/UTBM, Site de Montb´eliard, F-90010 Belfort, France

Abstract:

The development of high-efficiency cathode materials is critical for advancing the largescale commercialization of metal-supported solid oxide fuel cells (MS-SOFCs). In this study, Pr-Ni-O oxides were deposited using RMS and subsequently annealed at 1000°C for 30 min to induce the in-situ formation of a Pr₂NiO₄@Pr₆O₁₁ (PPNO) composite cathode. The incorporation of Pr₆O₁₁ mitigates the decomposition of Pr₂NiO₄ (PNO), thereby enhancing its long-term stability. Compared to the parent material PNO, the PPNO composite demonstrated superior electrocatalytic performance. The polarization resistance (R_n) of the PPNO cathode was significantly reduced to 0.07 $\Omega \cdot cm^2$, much lower than the 0.84 Ω ·cm² observed for PNO at 750°C. Furthermore, a single cell with the configuration ITM/GDC10/NiO-YSZ/8YSZ/GDC10/PPNO (MS/PPNO) exhibited remarkable maximum power density (Pmax) of 1010 mW·cm² at 750°C, compared to 326 the corresponding ITM/GDC10/NiO-YSZ/8YSZ/GDC10/(MS/PNO) configuration. These findings provide valuable insights into designing improved cathode layers for MS-SOFC applications.

Keywords:

MS-SOFC, PPNO, Composite cathode, RMS

* Corresponding authors at: Faculty of Metallurgical and Energy Engineering, Kunming University of Science and Technology, Kunming 650093, China.

E-mail addresses: 20040051@kust.edu.cn (S. GUO), 20230149@kust.edu.cn (K. CHEN).

1. Introduction:

As the global energy and environmental crises worsen, the demand for efficient and clean power generation technologies is growing rapidly [1,2]. The solid oxide fuel cell (SOFC) is regarded as a highly promising energy conversion device capable of directly transforming the chemical energy of various fuels into electrical energy. It offers numerous ad-

vantages, including exceptional energy conversion efficiency, fuel flex-ibility, and low pollutant emissions [2-4]. Conventional SOFCs are designed to operate at high temperatures (800-1000°C), enabling efficient energy conversion and eliminating the need for precious metal electrodes [5]. However, this high-temperature operating environment also presents several challenges, including limitations on material selection (requiring relatively expensive ceramic materials), increased fabrication costs, and reduced cell life. Thus, extensive research efforts have been devoted to reducing the operating temperature to the inter-mediate range (IT-SOFCs, 600-800°C) while maintaining the perfor-mance and efficiency of the cells [6,7]. A significant benefit brought by the lower operating temperature is that metal materials, such as ferritic stainless steel, can be used as SOFC component materials, including support and connectors. The fundamental concept of metal-supported SOFCs (MS-SOFCs) is to support thin ceramic electrode and electrolyte layers on low-cost, durable metal materials. This approach significantly reduces the reliance on relatively expensive ceramic materials, thereby minimizing material costs and enhancing the structural strength of the cell. Nevertheless, operating at lower temperatures slows down the kinetics of the cathode oxygen reduction reaction (ORR), presenting a key challenge for maintaining performance [8,9]. As a result, the polariza-tion resistance of the cell increases dramatically, leading to a substantial drop in whole-cell performance [10]. Therefore, it is essential to develop cathode materials with high catalytic activity to enhance the perfor-mance of IT-SOFCs.

Recently, rare earth nickelate compounds (Ln_2NiO_4 , Ln = La, Pr, Nd) with the K_2NiF_4 -type structure have garnered significant interest as cathode materials for IT-SOFCs, owing to their excellent mixed ionic and electronic conductivity (MIEC) properties [11–14]. These cathodes, with MIEC properties, allow the ORR sites to extend throughout the bulk material rather than being limited to the Triple-Phase Boundary (TPB), thereby reducing electrode polarization. Notably, Pr_2NiO_4 exhibits the highest oxygen diffusion among the related rare earth nickelate com-pounds at intermediate temperatures, which enhances the ORR process [13,15]. Additionally, investigations have shown that composite cathodes containing Pr_6O_{11} consistently exhibit promising ORR perfor-mance, as Pr_6O_{11} significantly accelerates the oxygen surface exchange kinetics [16,17]. However, to the best of our knowledge, there are few research reports on composite cathodes made from Pr_6O_{11} and Pr_2NiO_4 . Given the potential synergistic effect between these two phases, the ORR performance of the Pr_2NiO_4 cathode could be enhanced through the formation of such a composite.

Ceramic powder routes such as screen-printing, tape-casting, and slurry coating are commonly employed to create the cathode layer for SOFC [18–20]. For example, Pr_2NiO_4 ink has been screen-printed onto anode-supported SOFCs as the cathode, followed by sintering at 1200°C in air for 2 h. However, prolonged sintering at such high temperatures is unfavorable for the fabrication of MS-SOFCs. Physical vapor deposition (PVD) has gained attention as a promising technique for low-temperature deposition in MS-SOFC fabrication. Magnetron sputtering (MS), a widely used form of PVD, has been extensively applied to deposit various coatings. While MS has been primarily utilized for depositing dense electrolyte or barrier buffer layers [21,22], previous research in our lab has demonstrated that this technique can also be used to deposit cathode layers by cosputtering multiple metal targets [23–25].

In this work, thin PPNO (approximately 8.1 μ m) composite cathodes and PNO (approximately 8.5 μ m) cathodes were deposited via RMS on a sputtering device equipped with a plasma emission monitoring (PEM) system. MS/PPNO and MS/PNO single cells were then fabricated. The morphology and structure of the PPNO and PNO cathodes were analyzed using scanning electron microscopy (SEM) and X-ray diffraction (XRD), respectively. The electrical and electrochemical properties of the cath-odes were examined using the four-probe method and electrochemical impedance spectroscopy (EIS). The performance of the single cells was evaluated through current-voltage-power (I-V-P) measurements and EIS analysis.

2. Experimental procedure

2.1 Experiment device

PPNO and PNO cathode coatings were deposited by co-sputtering Pr and Ni targets in an Alcatel SCM650 sputtering chamber, which is equipped with a plasma emission monitoring (PEM) system. The com-plete RMS system consists of several components, including the sput-tering chamber, vacuum system, hardware control unit, gas flow control system, pulsed DC generator, and the PEM system. The sputtering chamber is a cylindrical vessel with a height of 300 mm, an inner diameter of 620 mm, and a total volume of approximately 100 L. The vacuum system consists of a main pump and a secondary turbomolecular pump, which can achieve a vacuum lower than 10⁻⁴ Pa. A twochannel DC Pinnacle® Plus+ generator from Advanced Energy® serves as the power supply, which can adjust the pulse frequency from 5 to 350 kHz. The substrate holder with a diameter of 610 mm was placed at a draw distance of 70 mm from the target surface (Dt-s = 70 mm), and it can rotate at a rate of 14 Revolution Per Minute (RPM) driven by a motor. A pressure gauge with a display upper limit of up to 10⁻³ mBar was used to determine the vacuum in the sputtering chamber. A more accurate MKS Baratron pressure gauge was used to display the operating pressure (≈ 2.0 Pa) in the chamber during the deposition in real time. Pr and Ni targets with a diameter of 200 mm purchased from Ampere Industrie company were placed on a copper pedestal whose bottom was in contact with circulating cooling water, and a graphite sheet was placed between the target and the copper pedestal to improve electrical contact. An RMS process equipped with a PEM system was confirmed to allow greater deposition rates [20,22]. The PEM system consists of optical fiber probe, conducting optical fiber, spectrometer, and photomultiplier to obey computer management to monitor plasma emission spectra. The optical fiber probe was placed on the area close up to the Pr target to capture the spectral signals of the 422 nm Pr emission line. The spectral signals level intensity of the Pr target was adjusted by a software developed by Labview® to control the deposition process. The annealing treatment of the deposited samples was carried out under air in a standard furnace from Borel company.

2.2 Cell preparation

The PPNO/8YSZ/PPNO and PNO/8YSZ/PNO symmetric cells were prepared by depositing PPNO and PNO cathodes on both sides of the 8YSZ plate (Φ 11 × 0.5 mm) purchased from Neyco company, respectively. The schematic diagram of the magnetron sputtering process was shown in Fig. 1b. The detailed deposition parameters of PPNO and PNO cathodes were shown in Table 1. The deposited PPNO/8YSZ/PPNO and PNO/8YSZ/PNO

symmetric cells were then annealing at 1000°C for 30 min. The preparation process of MS/PPNO and MS/PNO single cells was shown in Fig. 1a. PPNO and PNO were deposited on the NiO-YSZ anode layer of the half-cell ITM/GDC10/NiO-YSZ/8YSZ/GDC10 and then annealed at 1000°C for 30 min to prepare the MS/PPNO and MS/PNO single cells. It should be pointed out that the half-cell ITM/GDC10/NiO-YSZ/8YSZ/GDC10 including the ITM substrate, GDC barrier layer, NiO-YSZ anode layer, and YSZ/GDC bielectrolyte layer has been deposited in an earlier stage and is not the primary focus of this work.

2.3 Characterization

The structure of the samples was determined using a BRUKER D8 X-Ray diffraction (XRD) equipped with a LynxEye linear detector and Co K α radiation (λ = 1.78897 Å). The device was operated at a voltage of 35 keV and a current of 40 mA. The scans were carried out at room temperature in a 2θ range of 20°-90° with a scan rate of 6°.min⁻¹ and a scan step of 0.02°. The SEM (JEOL JSM-7800F) equipped with an Energy Dispersive X-ray Spectroscopy (EDS) detector was used to characterize the morphology and the composition of various samples. The porosity of the PPNO and PNO coatings were quantified by analyzing the SEM images using ImageJ software. To reduce the error as much as possible, the porosity of each sample was obtained by taking the average value after analyzing 10 images. The XPS characterization was carried out by a K-Alpha+ device produced by Thermo Fisher Scientific, which operates under the high vacuum (2 × 10⁻⁷ mbar) with aluminum Ka monochromatized radiation at the 1486.7 eV X-ray photon source. The measurements of all samples were performed in constant analyzer energy mode with a pass energy of 50 eV. Charge calibration was per-formed based on the binding energy of the C_{1s} photoelectron peak at 284.8 eV. The electronic conductivity of PPNO and PNO coatings deposited on alumina substrate (Φ23mm) was measured by the four-probe method via a HP 3458 A multimeter according to previous work in laboratory [26].

A Garmy 1000E electrochemical workstation was used for EIS measurement of PPNO/8YSZ/PPNO and PNO/8YSZ/PNO symmetrical cells. Two sides of the symmetrical cell were connected to the platinum wire electrode soldering by commercial silver paste with an area of 0.2 cm². Then the symmetrical cells were placed in a furnace (OTF-1200×). The EIS measurement was performed between 600 and 750°C at an interval of 50°C within a frequency range of 0.1–10⁶ Hz under the applied voltage perturbation of 10 mV at an oxygen partial pressure of 0.2 atm. The collected EIS data were analyzed by ZView software. A CS1350 electrochemical workstation was used to collect the current-voltage discharge curve (I-V) of the MS/PPNO and MS/PNO single cells. The shape of the single cells is a square with a side length of 1.1 cm. The cathode and ITM of a single cell were connected to the electrochemical workstation through platinum wires. The cell was sealed by high tem-perature sealant to introduce H₂ and air into the anode and cathode sides, respectively, without gas leakage. Commercial silver pastes with area of 0.2 cm² was coated on the cathode as the current collector layer. The sealed cell was placed in a furnace (OTF-1200×). Initially, the mixed gas 5%H₂-N₂ was introduced to the anode side at a flow rate of 30 mL/min until 600°C. Then, the hydrogen concentration was gradually increased to 100 % H₂ at 750 °C, and the gas flow rate was increased to 60 mL/min. The anode layer was reduced at 750°C for 3 h in a pure H₂ atmosphere. At the same time, air was introduced to the cathode side at a flow rate of 40 mL/min. After the open circuit voltage (OCV) stabilized, the electrochemical measurement procedure was initiated from 750°C to 600°C at an interval of 50°C.

3. results and discussion

Pr-Ni-O oxides with different Pr/Ni atomic ratios were deposited on the GDC10 layer according to the parameters listed in Table 1. Subse-quently, PPNO (Pr/Ni = 2.42) and PNO (Pr/Ni = 1.70) were synthesized by annealing these Pr-Ni-O oxides at 1000°C for 30 min. As shown in Fig. 2a, the deposited Pr-Ni-O oxides were amorphous or nanocrystalline, while Pr₂NiO₄@Pr₆O₁₁ and NiO were crystallized after annealing treatment at 1000 °C for 30 min. After crystallization, the Pr-Ni-O oxide with a low Pr:Ni atomic ratio mainly contains Pr₂NiO4 and a trace amount of NiO. While the Pr-Ni-O oxide with a high Pr:Ni atomic ratio grew Pr₂NiO₄ and Pr₆O₁₁ through crystallization to form composite Pr₂NiO₄@Pr₆O₁₁ (PPNO). Further, The XRD patterns of PPNO and PNO were refined by FullProf software. For PNO cathode, a single Pr₂NiO₄ phase refinement was performed while ignoring traces of NiO. For the PPNO cathode, a refinement containing two phases of Pr_2NiO_4 and Pr_6O_{11} was carried out (Figs. 2b-d). The refinement results showed that the content of Pr₆O₁₁ phase in PPNO accounted for 37.09 wt%. Compared with PNO, the unit cell volume of Pr₂NiO₄ in PPNO was 373.865 Å³ less than that in PNO of 370.293 Å³. This may be due to the presence of Pr₆O₁₁ suppressing the coarsening of Pr₂NiO₄ grains, and this result was consistent with the report of Zhao et al. [27]. To test the stability, PPNO and PNO were subjected to a long-term annealing treatment at the SOFC operating temperature (750°C) for 50 h in air (Fig. 2a). After long-term annealing treatment, Pr₄Ni₃O_{9.85} and Pr₆O₁₁ appeared in the PNO, which may be derived from the decomposition of Pr₂NiO₄ [28]. While no decomposed secondary phase Pr₄Ni₃O_{9.85} was observed in the PPNO, it exhibited an interesting stability, probably due to the presence of Pr₆O₁₁ which suppressed the decomposition of Pr₂NiO₄.

As cathode, the porous morphology facilitates the transport of oxidizing gases. The results of observing the morphology of PNO and PPNO were shown in Fig. 3. Initially, the as deposited PNO and PPNO were dense (Fig. 3a, d, g, and j). After annealing treatment at 1000°C for 30 min, porous morphology was formed in PNO and PPNO (Fig. 3b, e, h, and k). However, the morphology of PNO and PPNO were significantly different. For PPNO cathode, the porous morphology appears to be formed by small particles embedded in the large particle skeleton (Fig. 3e and k). The EDS results show that the Ni content in the large particle skeleton of PPNO was higher than that in the small particle area, which can be inferred to be the enriched areas of Pr_2NiO_4 and Pr_6O_{11} , respectively (Figs. 3n and 4a). The large particles in PNO were inter-connected and formed small pores (Fig. 3b and h). The EDS results show that the distribution of Pr and Ni was uniform (Figs. 3m and 4b). Combined with the XRD results, it can be confirmed that PNO was mainly composed of Pr₂NiO₄ large particles (Figs. 3m). Different mor-phologies gave PPNO and PNO different pore structures. In addition to the small-diameter pores in the Pr₆O₁₁-rich region, there were also large-diameter pores formed by the Pr₂NiO₄ skeleton in PPNO. How-ever, there were only small-diameter pores in PNO, which causes the porosity of PNO $(31.3 \pm 0.4 \%)$ to be much lower than that of PPNO (43.9 \pm 0.5 %) (Table 2). After long-term annealing treatment, the morphology of PPNO and PNO remains basically unchanged, and their porosity decreases only slightly, which indicates the stability of the pore structure of PPNO and PNO (Fig. 3c, f, i, and l).

Fig. 5 demonstrates the morphology evolution of the PPNO with annealing treatment. Initially, the as deposited PPNO looks dense (Fig. 5a and b). After annealing treatment at 950°C for 30 min, a distinct porous (macro pores) morphology was formed as shown in

Fig. 5 (e) and (f). The formation of the porous morphology of the PPNO may have go through three stages. In the first stage, the atomic-scale defects of the as deposited coating were eliminated to form micro (nano) pores as the annealing proceeds (until 900°C). At this stage, only Pr_6O_{11} -rich phase with small particles was crystallized in the coating with increasing temperature. Then micro(nano) pores were aggregated into macro pores at 950°C in the second stage (Fig. 5g and h). Meanwhile, Pr_2NiO_4 -rich phase with large particles was crystallized in the region with relatively low Pr:Ni atomic ratio. In the third stage, macro pores are aggregated into large pores at 1000°C (Fig. 5 I and j). At the same time, the Pr_2NiO_4 phase continues to crystallize in the relatively low Pr:Ni atomic ratio region. The Pr_6O_{11} -rich phase prevents the further agglomeration of Pr_2NiO_4 -rich phase with large particles. This is similar to filling the porous Pr_6O_{11} -enriched with small particles between the Pr_2NiO_4 -rich particles inside the PPNO, effectively increasing the porosity of the PPNO. Different from PPNO, the Pr:Ni atomic ratio of PNO is uniform, and the crystallized Pr_2NiO_4 -rich phase continues to agglomerate without being blocked (Figs. 3a, b, g, h and 4b). which leads to lower porosity of PNO.

For the SOFC, the surface oxygen species of the cathode material is an important factor affecting the oxygen reduction reaction (ORR) ac-tivity. Here, the XPS of O_{1s} of PPNO and PNO annealed at $1000\,^{\circ}$ C for 30 min were collected to confirm their surface oxygen species (Fig. 6). Four distinct peaks were observed from the XPS spectra of the O_{1s} orbital. The peak at low binding energy of about 528.2 eV was consid-ered to belong to Olattice, while the peaks at high binding energy (529.7, 531.2, and 532.5 eV) belong to Osurface, represents O^{2-} , O^{-} , and O^{2-} , respectively [29,30]. A larger Osurface/Olattice ratio means stronger oxy-gen adsorption ability on material surface, which helps to promote ORR activity [31,32]. The percentage of peak areas assigned to Olattice and Osurface in PPNO and PNO were shown in Table 3. Obviously, PPNO has larger Osurface/Olattice ratio (7.15) than that of PNO (4.76), indicating that PPNO was expected to have better ORR activity.

It is well known that Pr₂NiO₄ has abundant interstitial and vacancy oxygen, which promotes oxygen ion conduction [33]. The electronic conductivity also determines whether it is suitable for MS-SOFC cathode working at intermedium temperatures. Here, the electronic conductivity of PPNO and PNO deposited on alumina plate was measured by the four-probe method. As shown Fig. 7, both PPNO and PNO exhibit semi-conducting conduction behavior in the temperature range from 300 to 900°C. In the whole temperature range, the conductivity of PNO was higher than that of PPNO, which indicates that the introduction of Pr₆O₁₁ reduces the electronic conductivity. This was attributed to the fact that Pr₆O₁₁, as a poor electron conductor, suppresses the electron conduction pathway in PPNO [34]. The maximum conductivity of the deposited PPNO was about 87 S/cm at 700°C, while that of PNO was about 109 S/cm at 650°C. The conductivity of some reported cathode materials was compared and listed in Table 4. The conductivity of the PNO cathode coating deposited in this work was close to that in the literature. There were few reports on the electrical conductivity of PPNO composites. Compared with Pr₂CuO₄@Pr₆O₁₁, the deposited PPNO materials have obvious advantages in electrical conductivity. In addi-tion, the activation energy calculated by the Arrhenius formula in Eq.(1) shows that PPNO and PNO have similar values. This may indicate that the introduction of Pr_6O_{11} did not change the carrier transport mechanism.

$$\sigma(T) = \frac{A}{T} exp\left(-\frac{E_a}{kT}\right)$$
 Eq1

where T, and k, A, and Ea refer to the absolute temperature, Boltzmann's constant, a preexponential factor, and activation energy, respectively. The electrochemical performances of PPNO and PNO cathodes were evaluated by analyzing the EIS of PPNO/8YSZ/PPNO and PNO/8YSZ/PNO symmetric cells, respectively. Fig. 8a and b correspond to the Nyquist plots of PPNO/8YSZ/PPNO and PNO/8YSZ/PNO symmetrical cells in the temperature range of 600–750°C with a step of 50°C, respectively. The LR1(CPE1//R2euaaCPE2//R3) equivalent circuit model was considered for fitting the Nyquist plot of PPNO/8YSZ/PNO and PNO/8YSZ/PNO symmetrical cells. After fitting the impedance diagram by the ZView software, the resistances attributed to different contribu-tions were used to calculate the polarization resistance (Rp), which re-flects the electrochemical performance of the cathode material. On the basis of the fitted data and using relations Eq. (2), the mean capacitance of each contribution from semicircle have been calculated.

$$C = R^{((1-n)/n)} \times CPE^{1/n}$$
 Eq.2

The Schouler-type representation was adopted for plotting the capaci-tive (C) effect of each contribution v.s. reciprocal temperature [37,38]. Such plotting was considered to provide a reference for interpreting a given impedance diagram. Typical Arrhenius plots were shown in Fig. 9a. For the Nyquist plots of the PPNO cathode at $600 \,^{\circ}$ C and $650 \,^{\circ}$ C (Figs. 8a and 9a), the lower capacitance ($1029 \,^{\circ}$ F) from R2 was attributed to the response of the electrolyte [39]. Therefore, R2 and R1 were combined as the electrolyte resistance, and Rp was equal to R3 as shown in Fig. 8a. From $700 \,^{\circ}$ C to $750 \,^{\circ}$ C, the capacitance corresponding to the first semicircle increases (10^{-5} – $10^{-3} \,^{\circ}$ F), which was attributed to the electrode response [40,41]. In this case, Rp = R2 + R3, and R1 was a response from the electrolyte. Whereas for the PNO electrode, the ca-pacitances response from R2 and R3 were $10^{-4} \,^{\circ}$ F and $10^{-2} \,^{\circ}$ F, respec-tively, which was attributed to the response of the electrode (Figs. 8b and 9b) [39,41]. Likewise, R1 was attributed to the response of the electrolyte for PNO. In this case, for PNO electrode, Rp was equal to R2 plus R3 at temperature from 600 to $750 \,^{\circ}$ C. Finally, the Rp of PPNO and PNO cathodes were listed in Table 5.

The Rp and activation energy (Ea) of the PPNO cathode was much lower than that of the PNO at the temperature range o from 600 to 750°C, which shows the obvious advantage of PPNO cathode. Compared with the PNO cathode, the PPNO cathode with higher porosity and higher Osurface/Olattice ratio may be the reason for its lower Rp [42]. Additionally, the accelerated oxygen surface exchange kinetics of by Pr6O11 was also an important reason for the low resistance of PPNO cathode [43,44]. Table 5 also lists some reports on PNO and Pr_6O_{11} modified cathodes. The Rp of the deposited PNO cathode was higher than that reported in the literature. Only at a higher temperature of 750°C, its Rp of 0.84 $\Omega \cdot \text{cm}^2$ was close to that reported by J. FONDARD et al. of 0.8 $\Omega \cdot \text{cm}^2$ [26]. This may be related to the morphology of the deposited PNO cathode. While the deposited PPNO exhibited favorable competitiveness with low Rp of 0.07 $\Omega \cdot \text{cm}^2$ at 750°C. This may be attributed to the introduction of Pr_6O_{11} , which seems to have an important contribution in promoting the cathode ORR activity.

PPNO and PNO cathodes with similar thickness were deposited on the ITM/NiO-YSZ/8YSZ/GDC10 half-cell to assembled MS/PPNO and MS/PNO single cells, respectively. The single cell performance and microstructure were shown in Fig. 10 and Table 6. The maximum power density (Pmax) of MS/PNO increases from 133 mW·cm⁻² at 600 °C to 326 mW·cm⁻² at 750°C with increasing temperature, while the Pmax of

MS/PPNO increases from 390 mW·cm⁻² at 600°C to 1010 mW·cm⁻² at 750°C. The reason why the power output performance of MS/PPNO was much higher than that of MS/PNO should be attributed to the excellent electrochemical properties of PPNO composite cathode. It is worth mentioning that the developed MS/PPNO single cell shows competitiveness in Pmax compared with the reported MS-SOFCs (Table 7). However, the OCV of the developed MS/PPNO and MS/PNO cells were relatively lower than the literature reported in Table 7. And the OCVs of the developed MS/PPNO at the temperature range of 600–750°C were all within the most feasible fuel cell reversible voltage range of 0.8–1.5 V [49]. The reason for the lower OCV may be caused by the internal de-fects in the single cell. It can be seen from Fig. 10b and d that some microcracks exist in the electrolyte layers. In addition, the OCV of MS/PPNO was much lower than that of MS/PNO, which was due to the serious microcracks in both the 8YSZ and GDC10 electrolyte layers in MS/PNO, while only a few minor microcracks exist in the 8YSZ layer in MS/PNO. Serious microcracks may be inherited from the pit defects on the surface of manually polished NiO-YSZ anode layer, while minor microcracks generated during annealing treatment.

Long-term operational stability is crucial for the commercial application of MS-SOFC. The long-term durability of the MS/PPNO (represented in terms of cell voltage) at 700°C with a constant current load of 0.4 A/cm² as a function of operation time is used to evaluate the long-term performance of the single cell. After operation for 80 h, the voltage degradation rate of MS/PPNO only 4.1 % (decreased from 0.74 V to 0.71 V), which shows the outstanding long-term performance of MS/PPNO cell (Fig. 11a). Moreover, after long-term testing, each layer of the MS/PPNO single cell maintained structural stability, indicating that the single cell prepared by the all-physical deposition method has structural stability (Fig. 11b).

4. conclusion

Porous PPNO composites was facilely synthesized by RMS as the cathode material for MS-SOFCs. The Rp of the symmetric cell and the performance of the single cell show that the PPNO cathode exhibits higher electrocatalytic activity than the PNO cathode. The advantages of the PPNO cathode stem from its more favorable porous morphology and the enhanced ORR activity, facilitated by the incorporation of Pr_6O_{11} . The presence of Pr_6O_{11} phase helps inhibit the decomposition of Pr_2NiO_4 , which improving its stability. In PPNO, the initially crystallized Pr_6O_{11} prevents the later crystallized Pr_2NiO_4 from agglomerating, which is crucial for improving the porosity. The assembled MS/PPNO single cell demonstrates an output power of 1010 at $mW \cdot cm^2$ at $750 \circ C$, making it extremely competitive in the MS-SOFC field. These results highlight the potential of PPNO composites as SOFC cathodes and demonstrate the feasibility of fabricating MS-SOFC cathode layers via RMS. This work may offer new insights into the design of cathode layers for MS-SOFC applications.

CRediT authorship contribution statement

Xiaolei YE: Writing – original draft, Methodology, Investigation, Formal analysis, Data curation. Jiyun GAO: Writing – review & editing, Formal analysis. Shenghui GUO: Funding acquisition. Ming HOU: Formal analysis. Li Yang: Supervision, Funding acquisition, Conceptu-alization. Lei GAO: Formal analysis. Kaihua CHEN: Writing – review & editing,

Investigation, Formal analysis. Yunchuan LI: Software, Formal analysis. Pascal BRIOIS: Visualization, Formal analysis.

Declaration of competing interest

The authors declare the following financial interests/personal re-lationships which may be considered as potential competing interests: Xiaolei Ye reports financial support was provided by China Scholarship Council. Xiaolei Ye reports financial support was provided by Caiyun Postdoctoral Program in Yunnan Province of China. Shenghui GUO re-ports financial support was provided by National Natural Science Foundation of China. Li YANG reports financial support was provided by National Natural Science Foundation of China. If there are other authors, they declare that they have no known competing financial interests or personal relationships that could have appeared to influence the work reported in this paper.

Acknowledgments

The authors thank the China Scholarship Council (No. 201808530576), Caiyun Postdoctoral Program in Yunnan Province of China (CG24056E003A, CG24056E014A), National Natural Science Foundation of China (52364051, 52374389), Pays de Montbeliard Agglomeration.

Data availability

Data will be made available on request.

References

- [1] J. Gong, J. Hou, B-site high-entropy tailoring K_2NiF_4 oxide as an effective cathode for proton-conducting solid oxide fuel cells, J. Mater. Sci. Technol. 186 (2024) 158–163.
- [2] M. Fu, W. Hu, H. Tong, X. Ling, L.G. Tan, F.L. Chen, Z.T. Tao, Sn-doped cobalt containing perovskite as the air electrode for highly active and durable reversible protonic ceramic electrochemical cells, J. Adv. Ceram. 13 (1) (2024).
- [3] K.A. Kuterbekov, A.V. Nikonov, K.Z. Bekmyrza, N.B. Pavzderin, A.M. Kabyshev, M.
- M. Kubenova, G.D. Kabdrakhimova, N. Aidarbekov, Classification of solid oxide fuel cells, Nanomaterials 12 (7) (2022).
- [4] N. Dai, T. Shan, G. Wang, Z. Yang, Progress in preparation and application of rare earth based solid oxide fuel cell cathode materials, Chinese Rare Earths 44 (4)(2023) 58–70.
- [5] X. Deng, M. Zhang, Y. Gao, Fu Min, Q. Wang, Y.X. Zhu, Z.T. Tao, Balancing the triple conductivity of zinc-doped cathodes for proton-conducting solid oxide fuel cells, J. Mater. Chem. A 12 (29) (2024) 18175–18181.
- [6] Y.F. Tian, W.J. Wang, Y. Liu, L.L. Zhang, L.C. Jia, J. Yang, B. Chi, J. Pu, J. Li, Cobalt-free perovskite oxide $La_{0.6}Sr_{0.4}Fe_{0.8}Ni_{0.2}O_{3-\delta}$ as active and robust oxygen electrode for reversible solid oxide cells, Acs Appl. Energy Mater. 2 (5) (2019) 3297–3305.

- [7] C. Lim, A. Jun, H. Jo, K.M. Ok, J. Shin, Y.W. Ju, G. Kim, Influence of ca-doping in layered perovskite $PrBaCo_2O_{5+\delta}$ on the phase transition and cathodic performance of a solid oxide fuel cell, J. Mater. Chem. A 4 (17) (2016) 6479–6486.
- [8] J. Bai, L. Niu, Q. Zhu, D. Zhou, X. Zhu, N. Wang, W. Yan, J. Wang, Q. Liang, C.Wang, Ni-doped Fe-based perovskite to obtain multifunctional and highly efficient electrocatalytic active IT-SOFC electrode, Fuel 365 (2024).
- [9] D. Ding, X.X. Li, S.Y. Lai, K. Gerdes, M.L. Liu, Enhancing SOFC cathode performance by surface modification through infiltration, Energy Environ. Sci. 7 (2) (2014) 552–575.
- [10] S.B. Adler, Factors governing oxygen reduction in solid oxide fuel cell cathodes, Chem. Rev. 104 (10) (2004) 4791–4843.
- [11] A.P. Tarutin, A.R. Gilev, S.A. Baratov, G.K. Vdovin, D.A. Medvedev, Ba-doped $Pr_2NiO_{4+\delta}$ electrodes for proton-conducting electrochemical cells. Part 3: electrochemical applications, Int. J. Hydrogen Energ. 60 (2024) 261–271.
- [12] A.P. Tarutin, J.G. Lyagaeva, D.A. Medvedev, L. Bi, A.A. Yaremchenko, Recent advances in layered $Ln_2NiO_{4+\delta}$ nickelates: fundamentals and prospects of their applications in protonic ceramic fuel and electrolysis cells, J. Mater. Chem. A 9 (1)(2021) 154–195.
- [13] S. Yang, G. Liu, Y.-L. Lee, J.-M. Bassat, J. Gamon, A. Villesuzanne, J. Pietras, X.-D.Zhou, Y. Zhong, A systematic ab initio study of vacancy formation energy, diffusivity, and ionic conductivity of $Ln_2NiO_{4+\delta}$ (ln=La, Nd, Pr), J. Power Sources 576 (2023).
- [14] Z.Y. Han, J.H. Bai, X. Chen, X.F. Zhu, D.F. Zhou, Novel cobalt-free $Pr_2Ni_{1-x}Nb_xO_4$ (x=0, 0.05, 0.10, and 0.15) perovskite as the cathode material for IT-SOFC, Int. J. Hydrogen Energ. 46 (21) (2021) 11894–11907.
- [15] T. Nomura, S. Nishimoto, Y. Kameshima, M. Miyake, Electrode properties of doped PrNiO-based oxide cathode for intermediate-temperature SOFCs, J. Ceram. Soc. Jpn. 120 (1407) (2012) 534–538.
- [16] X.F. Tong, X. Xu, D. Tripkovic, P.V. Hendriksen, W.R. Kiebach, M. Chen, Promotion of oxygen reduction and evolution by applying a nanoengineered hybrid catalyst on cobalt free electrodes for solid oxide cells, J. Mater. Chem. A 8 (18) (2020) 9039–9048.
- [17] Y.H. Gu, Y.L. Zhang, Y.F. Zheng, H. Chen, L. Ge, L.C. Guo, $PrBaMn_2O_{5+\delta}$ with praseodymium oxide nano-catalyst as electrode for symmetrical solid oxide fuel cells, Appl. Catal. B-Environ. 257 (2019).
- [18] L.S. Mahmud, A. Muchtar, M.R. Somalu, Challenges in fabricating planar solid oxide fuel cells: a review, Renew. Sust. Energ. Rev. 72 (2017) 105–116.
- [19] E. Dogdibegovic, C.J. Wright, X.D. Zhou, Stability and activity of $(Pr_{1-x}Nd_x)_2NiO_4$ as cathodes for solid oxide fuel cells: I. Quantification of phase evolution in Pr_2NiO_4 , J. Am. Ceram. Soc. 99 (8) (2016) 2737–2741.
- [20] X.D. Zhou, J.W. Templeton, Z. Nie, H. Chen, J.W. Stevenson, L.R. Pederson, Electrochemical performance and stability of the cathode for solid oxide fuel cells:
- V.High performance and stable Pr_2NiO_4 as the cathode for solid oxide fuel cells, Electrochim. Acta 71 (2012) 44–49.
- [21] J. Nielsen, Å.H. Persson, T.T. Muhl, K. Brodersen, Towards high power density metal supported solid oxide fuel cell for Mobile applications, J. Electrochem. Soc. 165 (2) (2018) F90–F96.
- [22] P. Briois, F. Lapostolle, V. Demange, E. Djurado, A. Billard, Structural investigations of YSZ coatings prepared by DC magnetron sputtering, Surf. Coat. Technol. 201 (12) (2007) 6012–6018.

- [23] P. Briois, F. Perry, A. Billard, Structural and electrical characterisation of lanthanum nickelate reactively sputter-deposited thin films, Thin Solid Films 516 (10) (2008) 3282–3286.
- [24] J. Fondard, A. Billard, G. Bertrand, P. Briois, Synthesis and characterization of La_2NiO_4 coatings deposited by reactive magnetron sputtering using plasma emission monitoring, Solid State Ionics 265 (2014) 73–79.
- [25] J. Fondard, A. Billard, G. Bertrand, S. Fourcade, P. Batocchi, F. Mauvy, P. Briois, Effect of total pressure on La₂NiO₄ coatings deposited by reactive magnetron sputtering using plasma emission monitoring, Surf. Coat. Technol. 295 (2016) 29–36.
- [26] J. Fondard, A. Billard, G. Bertrand, P. Briois, Ln_2NiO_4 (ln = La, Pr, Nd) coatings deposited by reactive magnetron sputtering as cathode material for intermediate temperature solid oxide fuel cell, Vacuum 152 (2018) 97–108.
- [27] S. Zhao, N. Li, L. Sun, Q. Li, L. Huo, H. Zhao, One-pot synthesis Pr_6O_{11} decorated Pr_2CuO_4 composite cathode for solid oxide fuel cells, Int. J. Hydrogen Energ. 47 (9)(2022) 6227–6236.
- [28] V. Vibhu, A. Rougier, C. Nicollet, A. Flura, J.C. Grenier, J.M. Bassat, $La_{2-x}Pr_xNiO_{4+\delta}$ as suitable cathodes for metal supported SOFCs, Solid State Ionics 278 (2015) 32–37.
- [29] L. Liu, X. Zhou, Y. Wang, S. Li, R. Yin, P. Guo, J. Zhao, X. Zhao, B. Li, Composite ceramic cathode $La_{0.9}Ca_{0.1}Fe_{0.9}Nb_{0.1}O_{3-\delta}/Sc_{0.2}Zr_{0.8}O_{2-\delta}$ towards efficient carbon dioxide electrolysis in zirconia-based high temperature electrolyser, Int. J. Hydrogen Energ. 42 (22) (2017) 14905–14915.
- [30] Z.T. Tao, Y.M. Jiang, L. Lei, F. Chen, $Pr_{0.5}Ba_{0.5}Co_{0.7}Fe_{0.25}Nb_{0.05}O_{3-\delta}$ as air electrode for solid oxide steam electrolysis cells, Int. J. Hydrogen Energ. 44 (42)(2019) 23539–23546.
- [31] Q. Sun, L. Sun, Y. Dou, Q. Li, N. Li, L. Huo, H. Zhao, Insights into the oxygen reduction reaction on cu-doped SrFeO_{3- δ} cathode for solid oxide fuel cells, J. Power Sources 497 (2021).
- [32] H. Li, C. Su, C. Wang, Z. Lu, Electrochemical performance evaluation of FeCo₂O₄ spinel composite cathode for solid oxide fuel cells, J. Alloys Compd. 829 (2020).
- [33] Q. Zhou, Y. Gong, X. Zhang, Z. Xia, Synthesis and properties of Sr doped Pr₂NiO₄ cathode material for intermediate temperature solid oxide fuel cells, Ceram. Int. 50 (16) (2024) 28696–28706.
- [34] C. Nicollet, A. Flura, V. Vibhu, A. Rougier, J.-M. Bassat, J.-C. Grenier, An innovative efficient oxygen electrode for SOFC: Pr_6O_{11} infiltrated into Gd-doped ceria backbone, Int. J. Hydrogen Energ. 41 (34) (2016) 15538–15544.
- [35] V. Vibhu, A. Flura, C. Nicollet, S. Fourcade, N. Penin, J.M. Bassat, J.C. Grenier,
- A. Rougier, M. Pouchard, Characterization of PrNiO_{3- δ} as oxygen electrode for SOFCs, Solid State Sci. 81 (2018) 26–31.
- [36] E. Boehm, J.M. Bassat, P. Dordor, F. Mauvy, J.C. Grenier, P. Stevens, Oxygen diffusion and transport properties in non-stoichiometric $Ln_{2-x}NiO_{4+\delta}$ oxides, Solid State Ionics 176 (37–38) (2005) 2717–2725.
- [37] E. Schouler, M. Kleitz, Electrocatalysis and inductive effects at the gas, Pt/stabilized zirconia interface, J. Electrochem. Soc. 134 (5) (1987) 1045.
- [38] E. Schouler, N. Mesbahi, G. Vitter, In situ study of the sintering process of yttria stabilized zirconia by impedance spectroscopy, Solid State Ionics 9 (1983) 989–996.
- [39] S.B. Adler, Mechanism and kinetics of oxygen reduction on porous $La_{1-x}Sr_xCoO_{3-\delta}$ electrodes, Solid State Ionics 111 (1–2) (1998) 125–134.

- [40] F. Mauvy, C. Lalanne, J.-M. Bassat, J.-C. Grenier, H. Zhao, L. Huo, P. Stevens, Electrode properties of $Ln_2NiO_{4+\delta}$ (Ln= La, Nd, Pr): AC impedance and DC polarization studies, J. Electrochem. Soc. 153 (8) (2006) A1547.
- [41] J. Dailly, S. Fourcade, A. Largeteau, F. Mauvy, J.-C. Grenier, M. Marrony, Perovskite and A_2MO_4 -type oxides as new cathode materials for protonic solid oxide fuel cells, Electrochim. Acta 55 (20) (2010) 5847–5853.
- [42] W. Zhang, L. Zhang, K. Guan, X. Zhang, J. Meng, H. Wang, X. Liu, J. Meng, Effective promotion of oxygen reduction activity by rare earth doping in simple perovskite cathodes for intermediate-temperature solid oxide fuel cells, J. Power Sources 446 (2020) 227360.
- [43] X. Tong, Y. Xu, Đ. Tripkovi´c, P.V. Hendriksen, W.-R. Kiebach, M. Chen, Promotion of oxygen reduction and evolution by applying a nanoengineered hybrid catalyst on cobalt free electrodes for solid oxide cells, J. Mater. Chem. A 8 (18) (2020) 9039–9048.
- [44] Y. Chen, Y. Chen, D. Ding, Y. Ding, Y. Choi, L. Zhang, S. Yoo, D. Chen, B. Deglee,
- H. Xu, A robust and active hybrid catalyst for facile oxygen reduction in solid oxide fuel cells, Energy Environ. Sci. 10 (4) (2017) 964–971.
- [45] R.K. Sharma, N.I. Khamidy, J.M.Bassat, E.Djurado, $La_{2-x}PrxNiO_{4+\delta}$ -based efficient SOFC cathodes: effect of microstructure, composition and architecture, ECS Trans. 78 (1) (2017) 581.
- [46] C. Ferchaud, J.C. Grenier, Y. Zhang-Steenwinkel, M.M. Van Tuel, F.P. Van Berkel, J.M.Bassat, High performance praseodymium nickelate oxide cathode for low temperature solid oxide fuel cell, J. Power Sources 196 (4) (2011) 1872–1879.
- [47] B. Philippeau, F. Mauvy, C. Mazataud, S. Fourcade, J.C. Grenier, Comparative study of electrochemical properties of mixed conducting $Ln_2NiO_{4+\delta}$ (Ln= La, Pr and Nd) and $La_{0.6}Sr_{0.4}Fe_{0.8}Co_{0.2}O_{3-\delta}$ as SOFC cathodes associated to $Ce_{0.9}Gd_{0.1}O_{2-\delta}$, $La_{0.8}Sr_{0.2}Ga_{0.8}Mg_{0.2}O_{3-\delta}$ and $La_9Sr_1Si_6O_{26.5}$ electrolytes, Solid State Ionics 249 (2013) 17–25.
- [48] T. Ogier, F. Chauveau, J.M. Bassat, F. Mauvy, J.C. Grenier, J. Mougin, M. Petitjean, Enhanced performances of $Ln_2NiO_{4+\delta}/CGO$ multilayered anodes for high temperature steam electrolysis (HTSE), ECS Trans. 35 (1) (2011) 1817.
- [49] R. O'hayre, S.W. Cha, W. Colella, F.B. Prinz, Fuel cell fundamentals, John Wiley & Sons, 2016.
- [50] K. Li, Y.F. Jin, W.M. Gao, S.C. Xue, M. Zhang, Enhanced reliability of Ni-Fe alloys supported SOFCs with ex-situ sintered $La_{0.8}Sr_{0.2}MnO_{3-\delta}$ coated $Ba_{0.5}Sr_{0.5}Co_{0.8}Fe_{0.2}O_{3-\delta}$ cathode, J. Electrochem. Soc. 168 (3) (2021).
- [51] Y.M. Kim, P. Kim-Lohsoontorn, J. Bae, Effect of unsintered gadolinium-doped ceria buffer layer on performance of metal-supported solid oxide fuel cells using unsintered barium strontium cobalt ferrite cathode, J. Power Sources 195 (19)(2010) 6420–6427.
- [52] Q.A. Huang, J. Oberste-Berghaus, D. Yang, S. Yick, Z. Wang, B. Wang, R. Hui, Polarization analysis for metal-supported SOFCs from different fabrication processes, J. Power Sources 177 (2) (2008) 339–347.
- [53] D. Marcano, G. Mauer, R. Vaßen, A. Weber, Manufacturing of high performance solid oxide fuel cells (SOFCs) with atmospheric plasma spraying (APS) and plasma sprayphysical vapor deposition (PS-PVD), Surf. Coat. Technol. 318 (2017) 170–177.
- [54] J. Nielsen, Å.H. Persson, T.T. Muhl, K. Brodersen, Towards high power density metal supported solid oxide fuel cell for mobile applications, J. Electrochem. Soc. 165 (2) (2018) F90.

[55] M. Yoda, M. Echigo, Y. Tsuda, K. Minami, K. Manabe, H. Ohnishi, Power generation performance of a solid oxide fuel cell equipped with an Yttria-stabilized zirconia electrolyte formed over a support metal plate, J. Chem. Eng. Jpn 57 (1)(2024).

Figure caption:

- Fig. 1. The schematic diagram: (a) the preparation process of MS-SOFC single cells; (b) the working principle of reactive magnetron sputtering.
- Fig. 2. (a) XRD patterns of the PNO and PPNO cathodes as annealing treatment, (b) and (c) refined XRD patterns of the PNO and PPNO cathodes after annealing at 1000°C for 30 min, respectively, (d) structural parameters of the PNO and PPNO obtained after Rietveld refinement.
- Fig. 3. SEM images of the PNO and PPNO cathodes deposited on GDC10 layer: (a), (b), and (c) refer to the surface of as deposited PNO coating, annealing at 1000°C for 30 min, and 750°C for 50 h after annealing at 1000°C for 30 min, respectively; (d), (e), and (f) refer to the surface of as deposited PPNO coating, annealing at 1000°C for 30 min, and 750°C for 50 h after annealing at 1000°C for 30 min, respectively; (g), (h), and (i) refer to the cross-section of as deposited PNO coating, annealing at 1000°C for 30 min, and 750°C for 50 h after annealing at 1000°C for 30 min, respectively; (j), (k), and (l) refer to the surface of as deposited PPNO coating, annealing at 1000°C for 30 min, and 750°C for 50 h after annealing at 1000°C for 30 min, respectively; (m) and (n) refer to the mapping result of PNO and PPNO cathodes after annealing at 1000°C for 30 min.
- Fig. 4. SEM-EDS results of the PPNO and PNO coatings after annealing at 1000°C for 30 min
- Fig. 5. SEM images of the PPNO coatings after various annealing treatments:(a), (c), (e), (g), and (i) refer to the surface; (b), (d), (f), (h), and (j) refer to the cross-section.
- Fig. 6. XPS patterns of the coatings after annealing at 1000°C for 30 min: (a) PPNO, (b) PNO
- Fig. 7. Conductivity (a) and Arrhenius curves (b) of PNO and PPNO coatings deposited on alumina plate measured by four-probe method.
- Fig. 8. The EIS results of PPNO/8YSZ/PPNO and PNO/8YSZ/PNO symmetric cells at different temperature under the oxygen partial pressure of 0.2 atm, respectively.
- Fig. 9. (a) refer to the capacitance calculated according to the fitting result of EIS; (b) refer to Arrhenius plots of polarization resistances (Rp)
- Fig. 10. I-V-P curves of the single cells at various temperatures: (a) MS/PPNO, (c) MS/PNO; microstructure of the single cells after annealing at 1000°C: (b) MS/PPNO, (d) MS/PNO.
- Fig. 11. (a) The long-term performance of the MS/PPNO single cell under a constant current density of 0.4 A·cm⁻² for 80 h; (b) the microstructure of MS/PPNO single cells after long-term test.

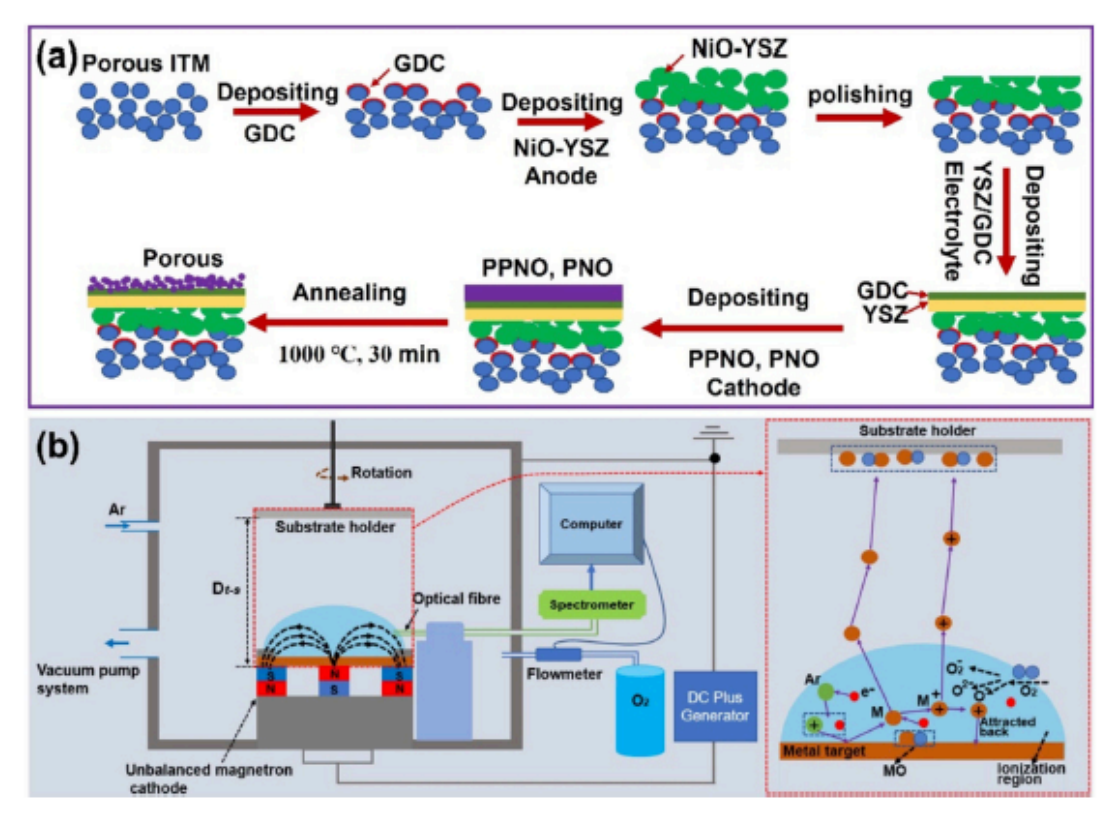


Fig 1

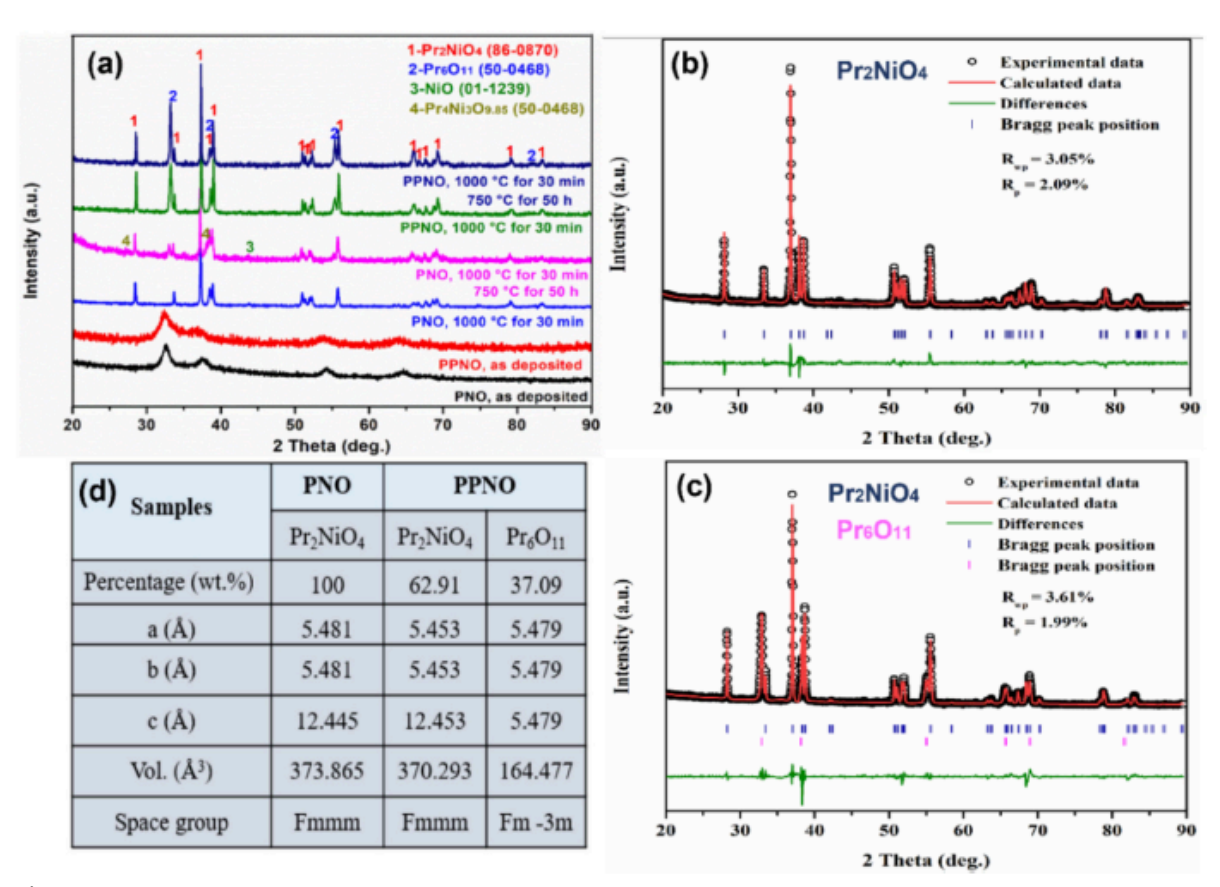


Fig 2

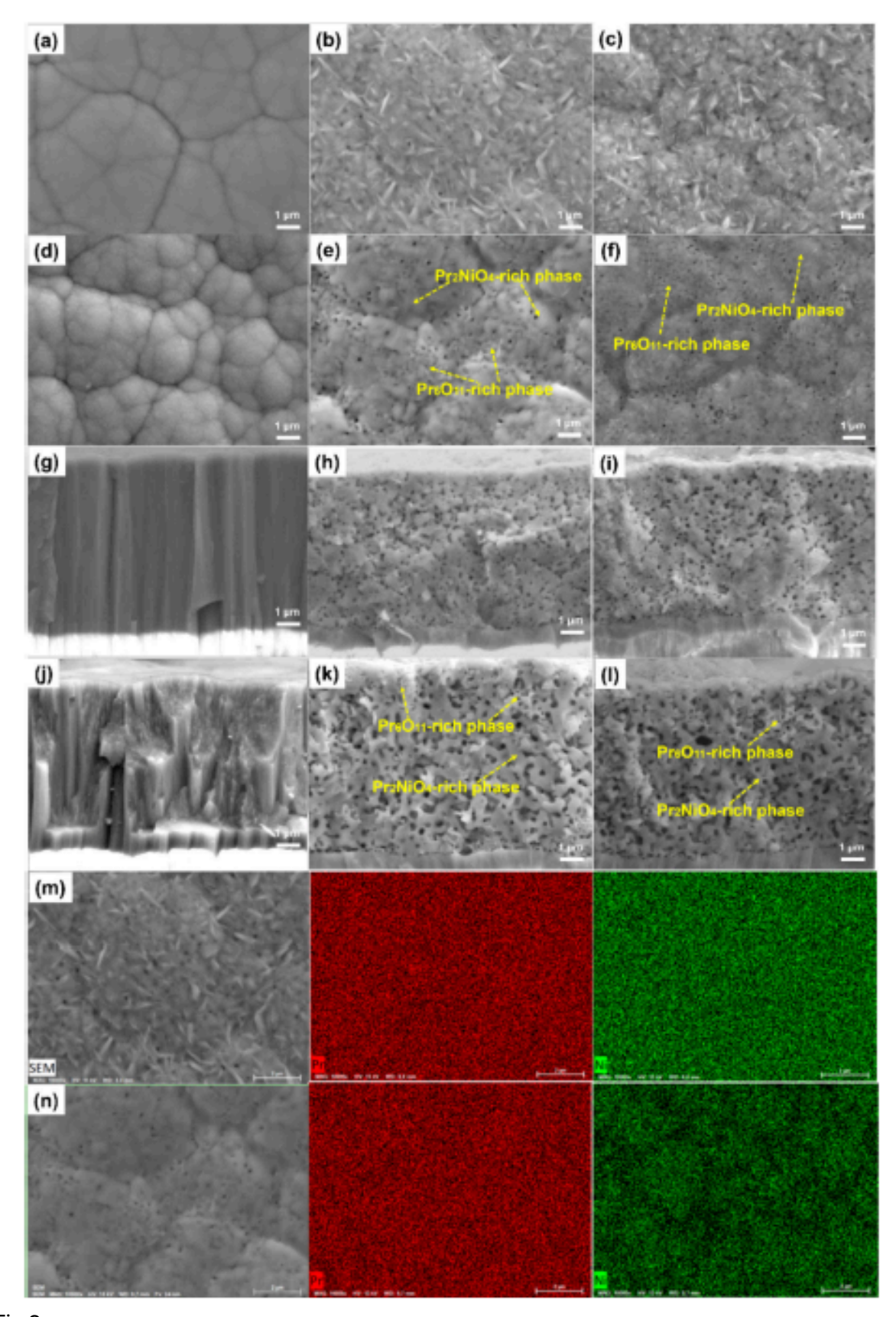


Fig 3.

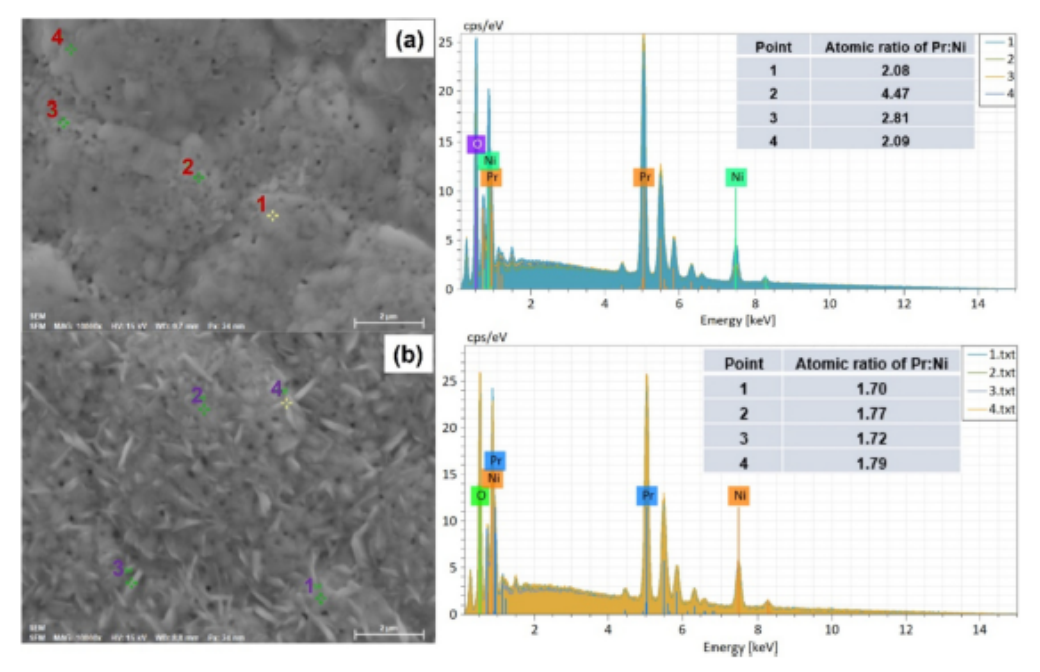


Fig4

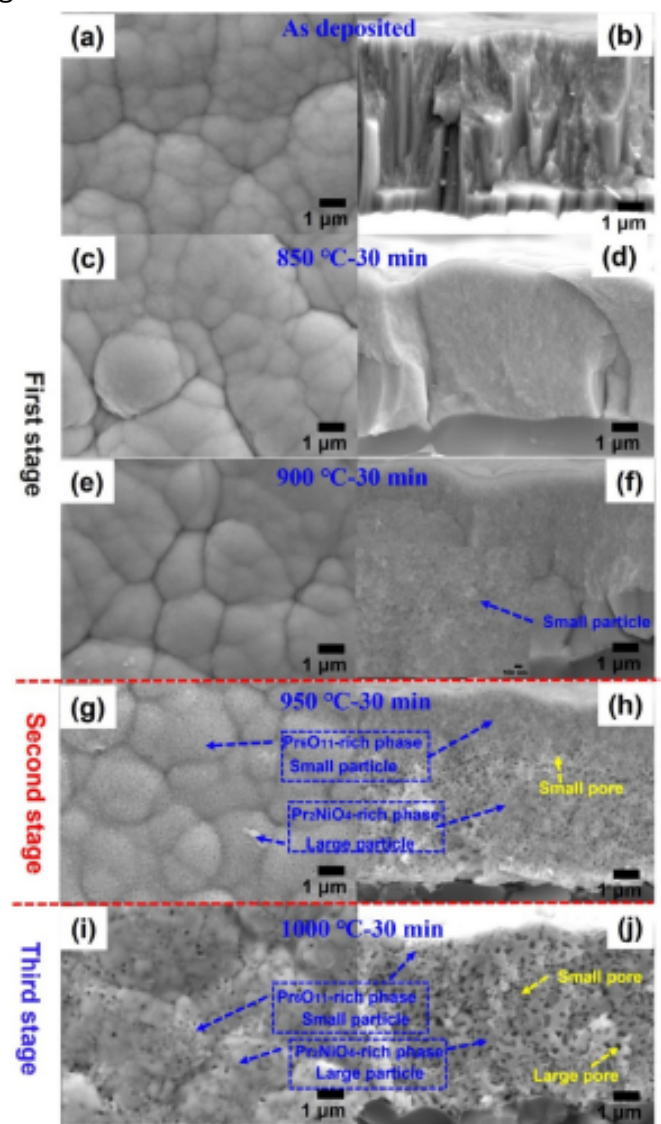


Fig5

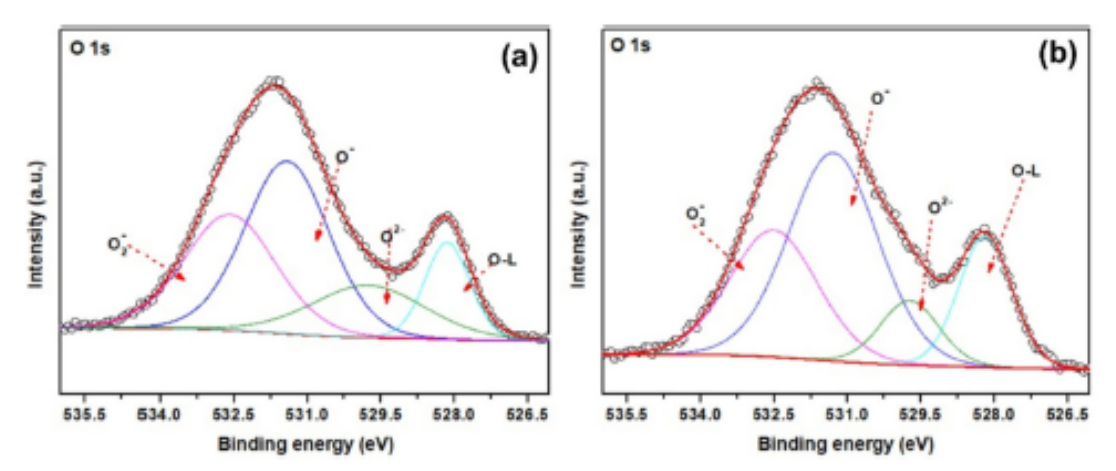


Fig6

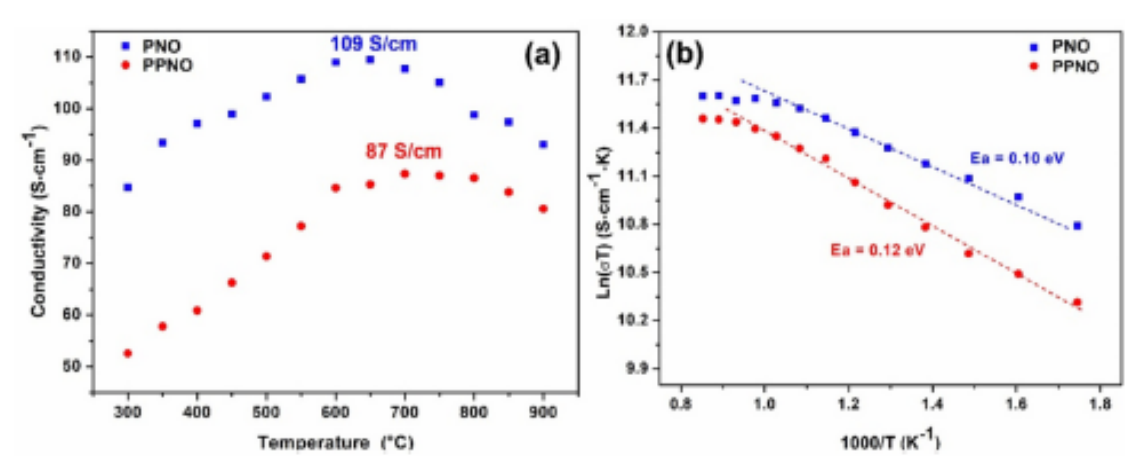


Fig7

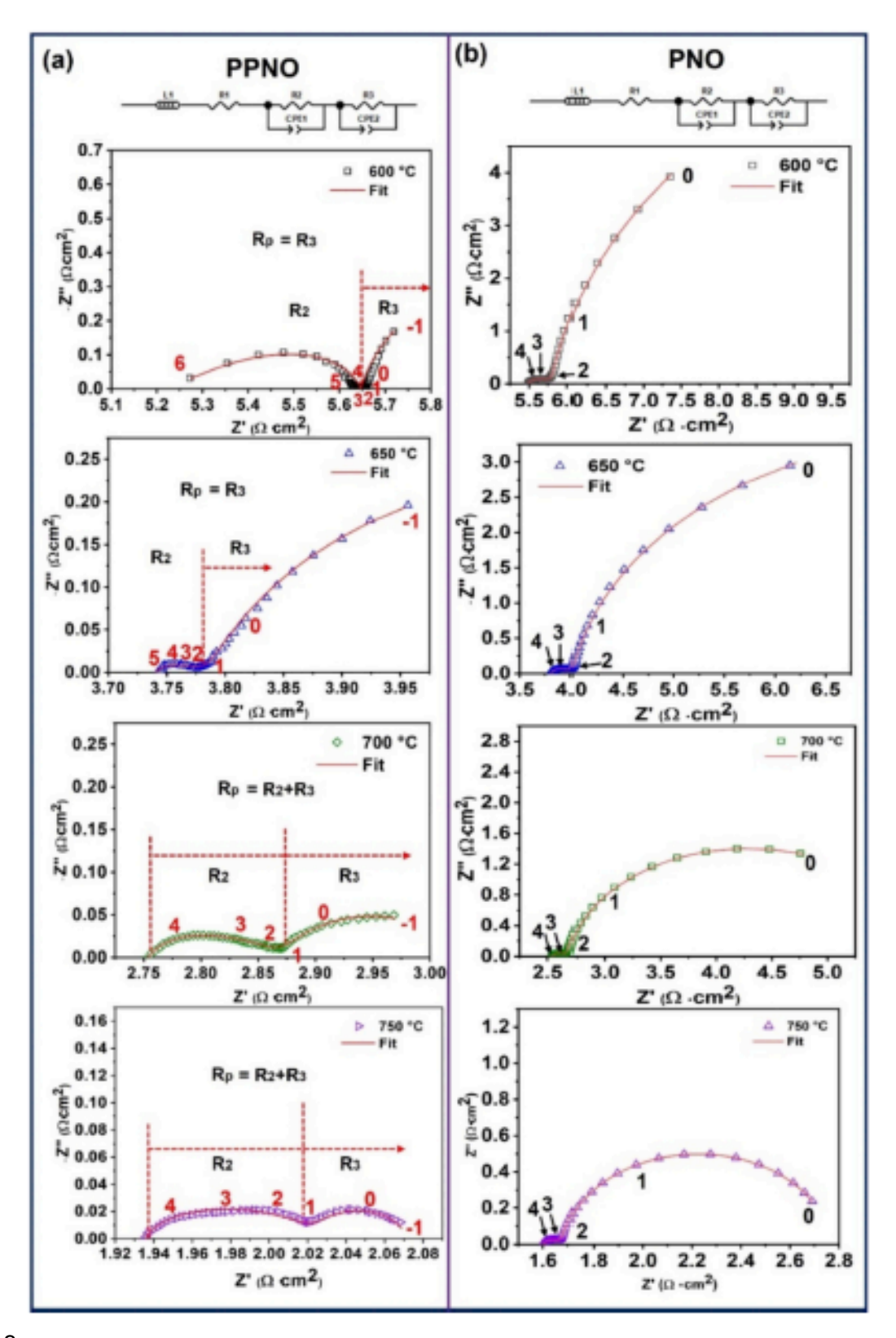


Fig 8

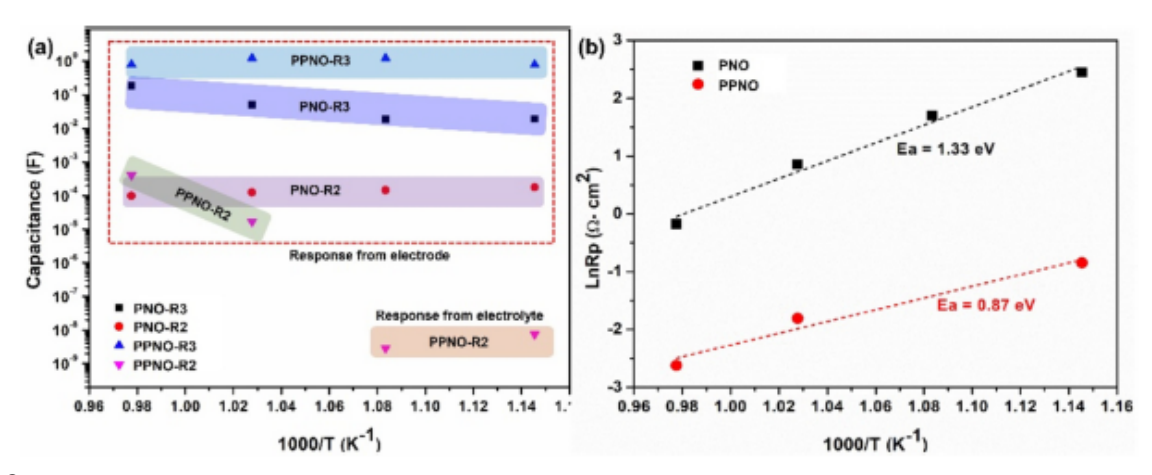


Fig9

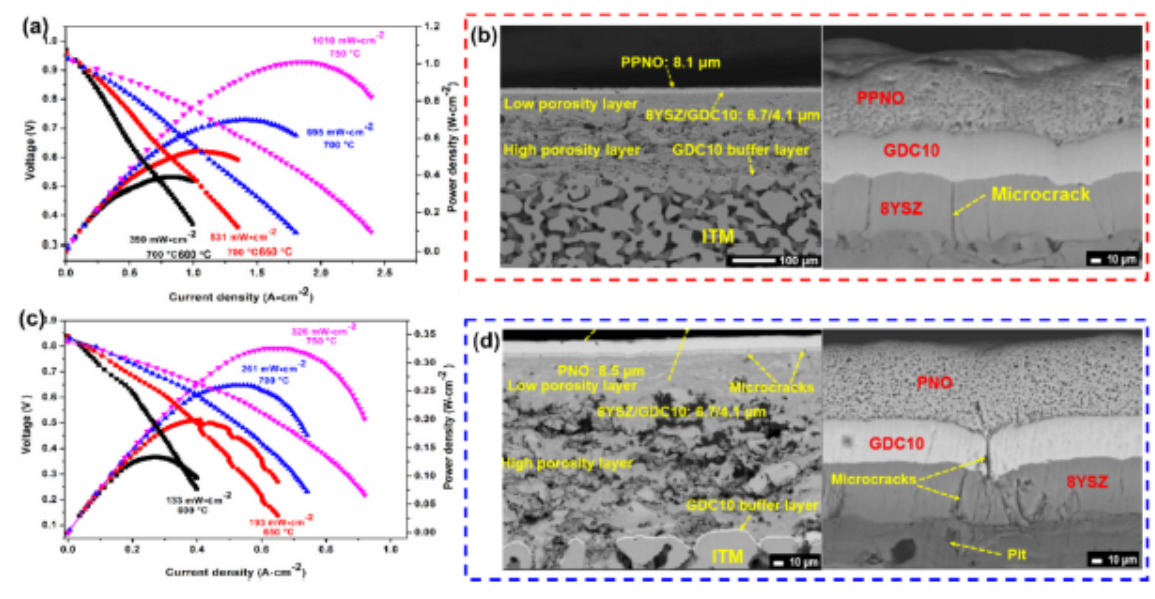


Fig10

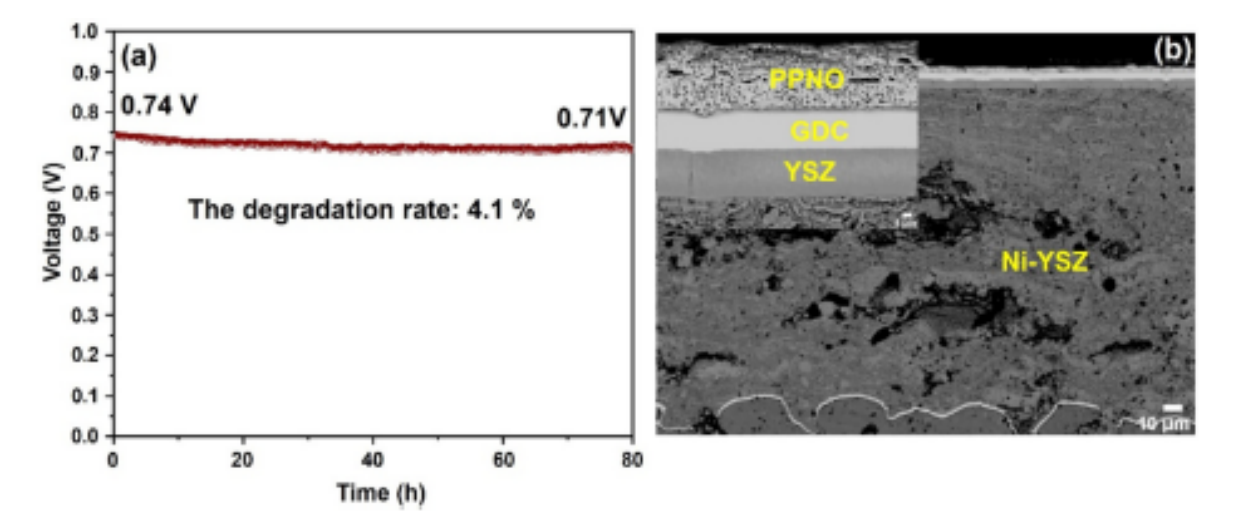


Fig11

Table of content:

Table 1
The deposition parameters to deposit PPNO and PNO cathode.

Deposition parameters		PPNO	PNO
Ar flow rate (see	m)	200	
O2 flow rate (seem)		4.9-5.2	4.9-5.3
Total pressure (Pa)		1.91-1.99	
Drawing distance(mm)		70	
Frequency (kHz)	50	
T _{off} (µs)		4	
Pr target	Spectral signals (%)	70	
	Current (A)	2.5	
Ni target	Power (W)	133	142
Deposition time (min)		140	170

Table 2
The cross-section porosity and thickness of the PPNO and PNO.

Cathodes	Cross-section porosity (Vol%)		
	1000 °C	1000 °C-30 min-750 °C-50 h	
PPNO	43.9 ± 0.5	42.6 ± 0.4	
PNO	31.3 ± 0.4	31.2 ± 0.4	

Table 3
The percentages of oxygen species of PPNO and PNO cathodes after annealing at 1000 °C for 30 min.

Oxygen species	PPNO	PNO
Osurface (%)	87.73	82.65
Olarrice (%)	12.27	17.35
O _{surface} / O _{lattice}	7.15	4.76

<u>Table 4</u>
The electronic conductivity of some cathode materials reported in the literature.

	Maximum conductivity (S/em)	Temperature (°C)	Refs.
Pr ₂ NiO ₄	119	600	[35]
Pr ₂ NiO ₄	106	450	[36]
Pr _{1.5} La _{0.5} NiO ₄	110	600	[28]
La ₂ NiO ₄	50	600	[28]
Pr ₂ CuO ₄	95	700	[27]
$Pr_2CuO_4@Pr_6O_{11}$	39	700	[27]

Table 5 The polarization resistances (R_p) of PPNO and PNO cathodes.

$R_p \; (\Omega {\cdot} cm^2)$ of symmetry cells	Temperature	(°C)		
	600	650	700	750
PNO/8YSZ/PNO	11.5	5.45	2.36	0.84
PPNO/8YSZ/PPNO	0.43	-	0.16	0.07
PNO/GDC/PNO			0.18 [14]	
PNO/GDC/PNO	0.83 [45]			
PNO/YSZ/YDC/PNO	0.32 [46]			
PNO/GDC/PNO	0.36 [47]			
PNO/LSGM/PNO	1.19 [47]			
PNO/YSZ/PNO				0.8 [26]
PNO/YSZ/PNO				0.18 [48]
PPCO/GDC/PPCO				0.07 [27]

PPCO: Pr2CuO4@Pr6O11.

Table 6
The OCV of the MS/PPNO and MS/PNO single cells at various temperatures.

Cells	OCV (V)			
	750 °C	700 °C	650 °C	600°C
MS/PPNO	0.941	0.939	0.960	0.968
MS/PNO	0.817	0.830	0.838	0.840

Table 7
Performance of some reported MS-SOFC.

Cell configuration	OCV (V)	$P_{max} (mW/cm^2)$	Refs.
Ni-Fe alloy/Ni-GDC/GDC/LSM-BSCF	0.86, H ₂	810 at 750 °C	[50]
STS430/Ni-YSZ/8YSZ/GDC/BSCF	1.082, 3%H ₂ O-H ₂	310 at 700 °C	[51]
SS430/Ni-SDC/ScSZ/GDC/SSC-GDC	0.98, 3%H ₂ O-H ₂	140 at 600 °C	[52]
ITM/GDC20/NiO-YSZ/8YSZ/GDC20/LNO	0.9, 5%H ₂ O-H ₂	76 at 700 °C	[25]
ITM/NiO-YSZ/YSZ/LSCF	1.058, 5%H ₂ O-H ₂	360 at 700 °C	[53]
Fe22Cr/Ni-YSZ/ScYSZ/LSC	1.06, 2%H ₂ O-H ₂	780 at 700 °C	[54]
Fe22Cr/Ni-GDC10/8YSZ/GDC10/LSCF	4.2 %H ₂ O-H ₂	850 at 750 °C	[55]